UC Irvine
UC Irvine Previously Published Works

Title
Reduced Model Captures Mg2+-RNA Interaction Free Energy of Riboswitches

Permalink
https://escholarship.org/uc/item/7jp4n46r

Journal
Biophysical Journal, 106(7)

ISSN
0006-3495

Authors
Hayes, Ryan L
Noel, Jeffrey K
Whitford, Paul C
et al.

Publication Date
2014-04-01

DOI
10.1016/j.bpj.2014.01.042

Peer reviewed

Reduced Model Captures Mg^{2+}-RNA Interaction Free Energy of Riboswitches

Ryan L. Hayes,[†] Jeffrey K. Noel,[†] Paul C. Whitford,[‡] Udayan Mohanty,[§] Karissa Y. Sanbonmatsu,[¶*] and José N. Onuchic[†‖*]

[†]Center for Theoretical Biological Physics and Department of Physics and Astronomy, Rice University, Houston, Texas; [‡]Department of Physics, Northeastern University, Boston, Massachusetts; [§]Department of Chemistry, Boston College, Chestnut Hill, Massachusetts; [¶]Theoretical Biology and Biophysics, Theoretical Division, Los Alamos National Labs, Los Alamos, New Mexico; and [‖]Department of Chemistry and Department of Biochemistry and Cell Biology, Rice University, Houston, Texas

ABSTRACT   The stability of RNA tertiary structures depends heavily on Mg^{2+}. The Mg^{2+}-RNA interaction free energy that stabilizes an RNA structure can be computed experimentally through fluorescence-based assays that measure Γ_{2+}, the number of excess Mg^{2+} associated with an RNA molecule. Previous explicit-solvent simulations predict that the majority of excess Mg^{2+} ions interact closely and strongly with the RNA, unlike monovalent ions such as K$^+$, suggesting that an explicit treatment of Mg^{2+} is important for capturing RNA dynamics. Here we present a reduced model that accurately reproduces the thermodynamics of Mg^{2+}-RNA interactions. This model is able to characterize long-timescale RNA dynamics coupled to Mg^{2+} through the explicit representation of Mg^{2+} ions. KCl is described by Debye-Hückel screening and a Manning condensation parameter, which represents condensed K$^+$ and models its competition with condensed Mg^{2+}. The model contains one fitted parameter, the number of condensed K$^+$ ions in the absence of Mg^{2+}. Values of Γ_{2+} computed from molecular dynamics simulations using the model show excellent agreement with both experimental data on the adenine riboswitch and previous explicit-solvent simulations of the SAM-I riboswitch. This agreement confirms the thermodynamic accuracy of the model via the direct relation of Γ_{2+} to the Mg^{2+}-RNA interaction free energy, and provides further support for the predictions from explicit-solvent calculations. This reduced model will be useful for future studies of the interplay between Mg^{2+} and RNA dynamics.

INTRODUCTION

The thermodynamics and kinetics of biological macromolecules like RNA and proteins can be described by energy-landscape theory. In an energy-landscape description, each highly populated configuration of the system corresponds to a basin of attraction on the energy landscape. Various features of the landscape explain different processes. Macromolecular folding requires a native energetic bias to guide the search for the native basin to overcome Levinthal's paradox and fold on biological timescales (1–3). This native bias implies that the free energy of a structure is determined largely by its similarity to the native structure. Such a landscape is well described by the principle of minimal frustration: native contacts are energetically stabilizing, and other contacts are less energetically significant (3).

Function occurs on the same landscape as folding, but frequently there are multiple basins of attraction within, and occasionally outside, the broader folded basin. To capture this functional frustration (4), inclusion of contacts and other information from these multiple basins is required (5). In some cases, the roughness of the landscape due to nonnative interactions is an important perturbation to the native-biased landscape (6,7). Nonspecific interactions, including electrostatics, are a source of frustration, because they stabilize interactions between both native and nonnative contacts. In proteins, electrostatic interactions can modulate the unfolded ensemble (8) and explain differences in thermodynamics and kinetics between homologous sequences (9). Although a minimally frustrated landscape is an apt baseline approximation for RNA with a native structure (10), frustration likely plays an even more important role in RNA than in proteins (11,12), including frustration and trapping that arise from electrostatic interactions (13,14). Indeed, the RNA energy landscape is quite electrostatically sensitive to the ionic environment (15,16), as the species and concentrations of ions in the ionic environment modulate the stability of competing structures. Modeling the ionic dependence of the RNA energy landscape is the focus of this work.

RNA is sensitive to the ionic environment because it is strongly negatively charged. For RNAs, such as riboswitches and ribosomal RNAs, to form compact structures that carry out biological function, counterbalancing RNA charge with cations such as Mg^{2+}, K$^+$, and Na$^+$ is essential. Mg^{2+} is especially effective in competing with other ions to balance RNA charge, because it is divalent and small. Although monovalent ions are generally present in much greater concentrations, only half as many Mg^{2+} ions as monovalent ions need to be localized to the region surrounding the RNA, which leads to a comparable entropic cost for localization. The small size of Mg^{2+} allows it to outcompete and displace larger divalent ions by approaching the RNA more closely (17–19).

Mg^{2+} plays a ubiquitous role in RNA stability and dynamics, and it exhibits many complex behaviors in the vicinity of RNA. A description of the ionic dependence of the landscape should encompass these features. Mg^{2+} is particularly effective at stabilizing compact RNA structures by inducing effective attraction between otherwise repulsive phosphates (13,19), and as a result, it plays a dramatic role in energetically stabilizing RNA tertiary structure (15). In turn, higher concentrations of Mg^{2+} tend to slow RNA kinetics by stabilizing compact structures (14,20). Explicit-solvent studies have suggested that Mg^{2+} fluctuations couple with RNA dynamics (21). This study also found that most Mg^{2+} associated with RNA is in the outer-sphere regime, separated from the RNA by one hydration layer (21). Ion-ion correlations in the dense outer-sphere regime are important for obtaining accurate free energies (22). Recent experimental studies of the SAM-I riboswitch have revealed a complex interplay between Mg^{2+} and S-adenosyl methionine (SAM) in stabilizing the SAM-I riboswitch (23). Modeling these features requires a more detailed representation of Mg^{2+} than of other ions. In this article, we focus on extending a minimally frustrated description of the landscape to include electrostatic frustration and ionic effects with an explicit representation of Mg^{2+}. The resulting model is able to accurately reproduce the thermodynamics of Mg^{2+}-RNA interaction.

A structure-based model (SBM) is an ideal way to represent a minimally frustrated landscape. In the simplest form, only native contacts are stabilized energetically, resulting in a smooth, native-biased landscape. The usefulness of this approximation is shown by the ability of such models to capture many aspects of protein (5,24–27) and RNA (28–33) folding and function. SBMs are also attractive from a modeling perspective due to their simplicity and rapid sampling. Smoother landscapes, together with underdamping (34), result in enhanced sampling approximately 10^4 times faster than explicit-solvent simulations (35,36). The simplicity of the SBM means that the effects of energetic perturbations like electrostatics on the overall native bias can be modeled and understood. In a pure SBM, electrostatic interactions and ions are only represented implicitly by their contribution to effective interactions of native contacts, and there is no ionic concentration dependence. To model the effects of ionic concentration dependence and of Mg^{2+} behavior in investigations of long-time dynamics of RNA, we design an SBM with explicit Mg^{2+} ions and an effective potential that implicitly represents KCl.

The energetic stabilization by Mg^{2+} is quantified by the Mg^{2+}-RNA interaction free energy, $\Delta G_{\text{Mg}^{2+}}$. Theoretical calculations have shown that in the presence of excess KCl, $\Delta G_{\text{Mg}^{2+}}$ is related to the excess Mg^{2+} (Γ_{2+}) according to

$$\Delta G_{\text{Mg}^{2+}} = -k_{\text{B}}T \int_0^{C_{2+}} \Gamma_{2+} d \ln C_{2+}, \qquad (1)$$

where both $\Delta G_{\text{Mg}^{2+}}$ and Γ_{2+} are functions of the Mg^{2+} concentration (C_{2+}) (37). The excess ions of an ionic species i per RNA molecule is a thermodynamic quantity called the preferential interaction coefficient, Γ_i (37), and varies with ionic concentration. Ionic subscripts i of 2+, +, and − refer to Mg^{2+}, K$^+$, and Cl$^-$, respectively. The charge of excess cations and depleted anions associated with the RNA must balance the RNA charge. Differences in $\Delta G_{\text{Mg}^{2+}}$ between conformational ensembles ($\Delta\Delta G_{\text{Mg}^{2+}}$) reveal preferential structural stabilization by Mg^{2+} that can be modulated by Mg^{2+} concentration.

Experimental curves for Γ_{2+} have been obtained for several systems using the fluorescent dye 8-hydroxyquinoline-5-sulfonic acid (HQS) (37). With these measurements, one can measure $\Delta\Delta G_{\text{Mg}^{2+}}$ between conformational ensembles (38,39) or characterize chelated Mg^{2+} binding in a specific site (40). Γ_{2+} has also been computed from microsecond-timescale explicit-solvent molecular dynamics simulations (21). Because the excess Mg^{2+} can be measured both experimentally and computationally, Γ_{2+} presents a powerful metric for uniting theory and experiment to build models of Mg^{2+}-RNA interactions. Furthermore, because of the relation between Γ_{2+} and $\Delta G_{\text{Mg}^{2+}}$, such models will be well parameterized thermodynamically.

In this study, we focus on two well characterized riboswitches to calibrate the model. Riboswitches are attractive systems for the study of Mg^{2+}-RNA interactions, because they are small and relatively simple but still possess many of the rich Mg^{2+}-sensitive tertiary interactions seen in larger systems (Fig. 1, B and D). Riboswitches are responsible for regulating a wide range of metabolic pathways in bacteria. These noncoding RNAs reside in the 5′ untranslated region and often control transcription of their mRNA by binding metabolites directly related to their protein product. Riboswitches have proved to be excellent systems to investigate RNA structure, function, and dynamics using a wide range of experimental (23,41–43) and computational techniques (21,30,44–48). The adenine riboswitch (Fig. 1, A and B) has been extensively studied experimentally (39,49–51), and Γ_{2+} data obtained by HQS titrations are available for Mg^{2+} concentrations ranging from 1 μM to 1 mM (39). The SAM-I riboswitch (Fig. 1, C and D) binds the SAM metabolite, and has been extensively studied experimentally (23,52,53) and computationally (21,30,54). Γ_{2+} for the SAM-I riboswitch has been computed in explicit-solvent studies (21).

Using thermodynamic data from these previous studies as a guide, we develop a model that incorporates ionic effects into SBMs. The model includes explicit Mg^{2+} ions that interact with the RNA through a Debye-Hückel potential, whereas KCl is represented implicitly through the screening length and a Mg^{2+}-dependent Manning condensation factor that scales RNA charge. We calibrate the model to accurately reproduce the preferential interaction
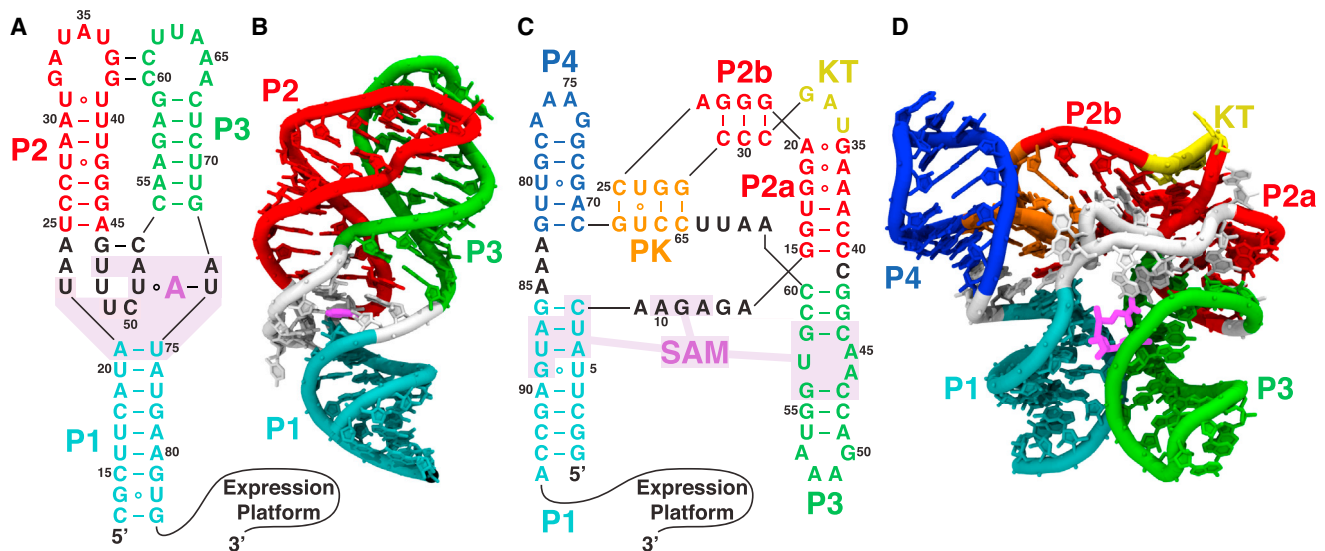
FIGURE 1 Secondary and tertiary structures of the two riboswitches used in this study. Mg^{2+} further stabilizes tertiary interactions induced by the metabolites. Metabolites are shown in magenta, and binding pockets are shaded. (*A* and *B*) Secondary (*A*) and tertiary (*B*) structures of the adenine riboswitch aptamer. The adenine metabolite stabilizes the tertiary interaction between the P2 and P3 helices. (*C* and *D*) Secondary (*C*) and tertiary (*D*) structures of the SAM-I riboswitch aptamer. The SAM metabolite stabilizes the tertiary interaction between the P3 helix and the nonlocal P1 helix, stabilizing the P1 helix and preventing strand invasion by the competing antiterminator helix in the expression platform. To see this figure in color, go online.

coefficient Γ_{2+} and the related Mg^{2+} interaction free energy, $\Delta G_{Mg^{2+}}$, in the native basin of these two riboswitches. The predictions for Γ_{2+} are consistent with experimental HQS measurements of the adenine riboswitch (39) and simulation results of the SAM-I riboswitch (21). With this hybrid structure-based model in hand, we are poised to address more sophisticated questions about the interplay of Mg^{2+}, ligands, and RNA during folding and function.

MODEL AND METHODS

Structure-based models

SBMs have been used extensively in studies of proteins (24,25,55), and in several studies of RNA (28,30,31,48). Previous studies have included electrostatic effects in the SBM of RNA. The simplest models utilize a repulsive Debye-Hückel interaction between phosphates (28,29). In these models, all ions are implicit. We utilize Debye-Hückel interactions and include explicit Mg^{2+} ions, because explicit counterions are required for Debye-Hückel interactions to produce the attractive effective phosphate-phosphate interactions that Mg^{2+} induces.

Although they still lack explicit counterions, more recent SBMs with electrostatics have added a scaling of RNA charge to Debye-Hückel interactions to account for Manning condensed ions (56). Manning counterion condensation is a useful theoretical tool for understanding the behavior of polyelectrolyte chains like RNA in solution (57,58). Manning counterion condensation theory was originally conceived as the low-concentration limiting behavior of an infinite line of charge in solution. If the linear charge spacing, b, is shorter than the Bjerrum length, l_B, the length scale where the electrostatic and thermal energy scales cross (see Eq. 10), ions will condense out of solution onto the RNA and effectively rescale the charge. Although Manning condensation was assumed to be constant in previous SBMs (56), we have developed

a model of Manning condensation that can vary with ionic concentration and allow separation of the condensed populations of Mg^{2+} and K^+. This separation is critical for capturing Mg^{2+} concentration effects, since condensed Mg^{2+} replaces condensed K^+, and hence the effective rescaling of RNA charge induced by K^+ diminishes as Mg^{2+} concentration increases.

The competition between condensed Mg^{2+} and KCl provides the interface between discrete and continuum treatments, and if it is modeled well, treating Mg^{2+} as discrete ions and KCl as a continuum inducing an effective potential is a reasonable approximation. Continuum models can capture KCl behavior well, but cannot capture Mg^{2+} behavior because ion-ion correlations become important (59). Continuum approaches break down when the electrostatic coupling parameter (60) approaches unity (see Section S3 in the Supporting Material). The electrostatic coupling parameter varies like the surface charge density and the ion valency squared. Thus, the coupling parameter is four times higher for Mg^{2+} than for K^+. Although the surface charge density of RNA is hard to estimate, the success of continuum models with KCl and their failure with Mg^{2+} suggests that RNA is in the intermediate regime where the electrostatic coupling parameter of Mg^{2+} is greater than one, whereas for K^+ it is less than one. This is the regime to which a discrete Mg^{2+} and continuum KCl model is best suited.

We modify an all-atom SBM (30,55), which explicitly includes all heavy atoms, to include explicit Mg^{2+} ions and electrostatic interactions. Explicit Mg^{2+} ions are included to properly represent Mg^{2+}-induced phosphate attraction, Mg^{2+}-Mg^{2+} correlation, and the dense outer-sphere Mg^{2+} population. KCl screening is represented by a Debye-Hückel potential with a Mg^{2+}-dependent KCl Manning condensation factor. The functional form of the potential is

$$V = V_{SBM} + V_{Mg\text{-}Size} + V_{ES}, \qquad (2)$$

where V_{SBM} is the all-atom SBM potential containing the minimally frustrated native bias, $V_{Mg\text{-}Size}$ controls the size of the explicit Mg^{2+} ions, and V_{ES} contains the effective electrostatic interactions. Simulation input files can be obtained at http://smog-server.org/forcefields. V_{SBM} is given by

$$V_{\text{SBM}} = \sum_i^{\text{bonds}} \frac{\epsilon_r}{2}(r_i - r_{0i})^2 + \sum_i^{\text{angles}} \frac{\epsilon_\theta}{2}(\theta_i - \theta_{0i})^2$$

$$+ \sum_i^{\substack{\text{impropers} \\ \text{or planar}}} \frac{\epsilon_\chi}{2}(\chi_i - \chi_{0i})^2$$

$$+ \sum_i^{\substack{\text{proper} \\ \text{dihedrals}}} \epsilon_\phi F_{\text{D}}(\phi_i - \phi_{0i}) \qquad (3)$$

$$+ \sum_{ij}^{\text{contacts}} \epsilon_{\text{C}} \left(\left(\frac{\sigma_{ij}}{r_{ij}}\right)^{12} - 2\left(\frac{\sigma_{ij}}{r_{ij}}\right)^6 \right)$$

$$+ \sum_{ij}^{\substack{\text{RNA-RNA} \\ \text{non-contacts}}} \epsilon_{\text{NC}} \left(\frac{\sigma_{\text{NC}}}{r_{ij}}\right)^{12},$$

where

$$F_{\text{D}}(\phi) = (1 - \cos\phi) + \frac{1}{2}(1 - \cos 3\phi). \qquad (4)$$

Geometric parameters (r_{0i}, θ_{0i}, χ_{0i}, ϕ_{0i}, and σ_{ij}) are set by their values in a crystal structure, so that the crystal structure is the global minimum in energy. Energetic parameters have been calibrated (30,55) and are listed in Section S1 in the Supporting Material. The shadow method (61) was used to obtain the contact map for the sum over contacts. The final term controls the excluded volume and enforces steric constraints. Excluded-volume parameters are given by $\sigma_{\text{NC}} = 1.7$ Å and $\epsilon_{\text{NC}} = \epsilon_{\text{R}}$, where $\epsilon_{\text{R}} = 1.5\, k_{\text{B}}T$ is the reduced energy unit (see Section S1 in the Supporting Material), and T is the simulation temperature of 300 K.

The excluded volume of the Mg^{2+} ions is controlled by $V_{\text{Mg-Size}}$, which is given by

$$V_{\text{Mg-Size}} = \sum_{ij}^{\text{Mg-RNA}} \epsilon_{\text{MgRNA}} \left(\frac{\sigma_{\text{MgRNA}}}{r_{ij}}\right)^{12}$$

$$+ \sum_{ij}^{\text{Mg-Mg}} \epsilon_{\text{MgMg}} \left(\frac{\sigma_{\text{MgMg}}}{r_{ij}}\right)^{12}. \qquad (5)$$

Parameters are calibrated in the first subsection under Results. For $\epsilon_{\text{MgRNA}} = \epsilon_{\text{MgMg}} = \epsilon_{\text{R}}$, it is determined that $\sigma_{\text{MgRNA}} = 3.4$ Å and $\sigma_{\text{MgMg}} = 5.6$ Å.

The electrostatic potential is given by

$$V_{\text{ES}} = \sum_{ij}^{\substack{\text{Mg-RNA} \\ \text{Mg-Mg}}} \frac{1}{4\pi\epsilon_0\epsilon} \frac{\alpha_i q_i \alpha_j q_j}{r_{ij}} \exp\left(-\frac{r_{ij}}{l_{\text{D}}}\right), \qquad (6)$$

where the dielectric constant $\epsilon = 80$ mimics water, ϵ_0 is the permittivity of free space, l_{D} is the Debye length (excluding Mg^{2+} screening), and α is the Manning condensation prefactor that rescales the charges q due to the presence of implicit condensed K$^+$. Note that the sum includes only Mg^{2+}-RNA and Mg^{2+}-Mg^{2+} interactions. Since the SBM already implicitly includes native RNA-RNA interactions in V_{SBM}, such as hydrogen bonding and base-pairing interactions, RNA-RNA electrostatic interactions were excluded to avoid double counting. Since RNA-RNA electrostatic interactions are excluded, the model can only capture the indirect effect of KCl upon the Mg^{2+} dependence of the RNA energy landscape. This model is most appropriate at intermediate KCl concentrations where the native basin is stabilized by KCl. A different model of RNA-RNA electrostatic interactions that can overcome the native bias of V_{SBM} would be required to capture the full KCl dependence of the energy landscape, such as unfolding under low salt conditions.

Previous studies have shown that the Mg^{2+} distribution is controlled by many negatively charged atoms on the RNA, as opposed to only the phos-

phates (21,62). Since hydrogens are not represented in the SBM, united atom charges were placed on every heavy atom to reproduce the electrostatic potential and resultant Mg^{2+} distribution. United atom charges were obtained from Amber 99 (63) by adding all hydrogen charges to the nearest heavy atom. This approximation does not alter the charge of any atoms that interact strongly with Mg^{2+}, with the possible exception of OH2$'$, which interacts moderately (21).

The Debye length in V_{ES} is given by

$$l_{\text{D}} = \sqrt{\frac{\epsilon\epsilon_0 k_{\text{B}} T}{\sum_i q_i^2 n_i}}, \qquad (7)$$

where n_i and q_i are the number density and charge of ionic species i, and k_{B} is the Boltzmann constant. To compute l_{D} for V_{ES}, Mg^{2+} is excluded from the sum over ionic species i, because Mg^{2+} is accounted for explicitly. The Manning condensation prefactor is given by

$$\alpha_i = \begin{cases} 1 - \theta_+ & i = \text{RNA} \\ 1 & i = \text{Mg}^{2+} \end{cases}. \qquad (8)$$

θ_+ is the number of Manning condensed K$^+$ per phosphate, which is explained in the second subsection under Results. Thus, α rescales the RNA charge due to the presence of implicit condensed K$^+$, leaving the Mg^{2+} charge unchanged. Since SBMs use reduced units, V_{ES} is multiplied by the conversion factor in Eq. S3 to convert from kJ/mol to reduced energy units. The conversion factor was determined by noting that a temperature of 80 T_{R} in simulation units corresponded to 300 K and then equating thermal energy scales. This conversion resulted in an ionic distribution appropriate to 300 K within our simulations. See Section S1 in the Supporting Material for more details.

Molecular dynamics simulations

Simulations were run using the Gromacs-4.6.1 molecular dynamics package (64). Langevin dynamics in the underdamped limit were used as a thermostat (see Section S1 in the Supporting Material for details). Implicit KCl concentrations of 50 mM (adenine riboswitch) and 100 mM (SAM-I riboswitch) were chosen for direct comparison with previous experiments (39) and simulations (21) on these systems. Simulations were run at varying concentrations of explicit Mg^{2+}. Cubic boxes were chosen such that the box was at least 500 Å on a side, but also such that there was a minimum of 200 bulk Mg^{2+} ions in the box, in addition to the Γ_{2+} Mg^{2+} ions associated with the RNA. For the most dilute simulations (10^{-6} M Mg^{2+}), this resulted in boxes 7000 Å on a side. Such low Mg^{2+} concentrations are completely inaccessible with explicit-solvent simulations, but have little effect on the computational expense of this model. Production simulations at each Mg^{2+} concentration were run for 2.5×10^8 time steps.

Nonlinear Poisson-Boltzmann calculations

Two theoretical models have been used extensively in studies of RNA: nonlinear Poisson-Boltzmann (NLPB) theory (65,66) and Manning counterion condensation theory (57,67). Poisson-Boltzmann methods have played a critical role in shedding light on RNA electrostatics. These methods have been advanced by the seminal contribution of Baker and co-workers, whose methods have enabled rapid calculation of electrostatic potentials for very large molecules (68–70). NLPB treats ions in a mean-field manner, which neglects ion-ion correlations (22,71) and ion size effects (59,72,73). NLPB has been successfully applied to many systems (66,74) and predicts $\Delta\Delta G_{\text{Mg}^{2+}}$ within computational uncertainty (75,76). Although NLPB accurately predicts $\Delta\Delta G_{\text{Mg}^{2+}}$, values for Γ_{2+} and $\Delta G_{\text{Mg}^{2+}}$ are systematically low by ~25%. We choose not to use NLPB directly in our SBM, partly because removing the double counting of RNA-RNA electrostatic interactions implicitly represented in the contact terms is not

straightforward with NLPB and partly because of the systematically low values of Γ_{2+} and $\Delta G_{Mg^{2+}}$ given by NLPB calculations. NLPB calculations are used to corroborate the model and parameters obtained for Manning condensed K^+ in the second subsection under Results. NLPB calculations were performed using the adaptive Poisson-Boltzmann solver (APBS) (68), with parameters listed in Section S2 in the Supporting Material.

The NLPB equation determines the potential by assuming that the mean ionic density fields are governed by the Boltzmann distribution. The linearized Poisson-Boltzmann (LPB) equation is obtained by linearizing the Boltzmann distribution around zero potential. The Debye-Hückel (DH) approximation is further obtained by neglecting the solute's dielectric constant and ionic accessibility. Both LPB and DH are described by homogenous differential equations, and thus the solution may be multiplied by a coefficient α. By Gauss' law, $\alpha = 1 - \sum_i z_i \theta_i$, where z_i is the valence and θ_i is the Manning condensed fraction per phosphate of the ionic species i. This implies that the excess ions, Γ_i, may be split into a population that screens and a population that condenses.

The total condensed charge, $\sum_i z_i \theta_i$, may be obtained by fitting either LBP or DH to NLPB far from the RNA, where the potential is small and the linearized Boltzmann distribution is valid. In this case, fitting was performed at a set of points within a 240 Å box but outside a 120 Å box centered on the RNA. The condensed ions obtained by LPB and DH fits are identical at low concentrations but begin to differ near the 50 mM concentrations used in this study. Fitting to Debye-Hückel is used because that is more appropriate to the form of the potential used in Eq. 6, but for completeness, fits to both are shown in Fig. S1 in the Supporting Material.

To partition the Manning condensed ions by species, ion densities were computed from the full NLPB and scaled DH potentials. The difference in ion densities integrated over all space gives the condensed ions for that species. At high ionic concentrations, this also results in a nonzero condensation of Cl^-. This occurs because the linearized potential predicts a nonphysical negative density in regions of strong potential, but NLPB gives approximately zero density.

RESULTS

Calibration of Mg^{2+} ion size

Previous studies have shown that the affinity between an ion and RNA is strongly dependent on ion size (17–19,77). Given $\epsilon_{MgRNA} = \epsilon_{MgMg} = \epsilon_R$, the effective size of Mg^{2+} is controlled by σ_{MgRNA} and σ_{MgMg} in the excluded-volume term. Because the ionic affinity for RNA is sensitive to ion size, these parameters must be carefully calibrated to accurately predict Γ_{2+}.

Explicit-solvent simulations have shown that most excess Mg^{2+} resides in the outer-sphere peak between 3.5 and 5 Å from the RNA, separated by a single hydration layer (21). In this model, the position of this peak is controlled by the values of σ_{MgRNA} in the excluded volume term (Eq. 5) and by the electrostatic potential (Eq. 6). To deconvolute the calibration of the Mg^{2+} excluded volume from the calibration of implicit Manning condensed KCl, excluded volume calibrations were performed in the high Mg^{2+} concentration regime (10 mM Mg^{2+} vs. 100 mM K^+) where negligible KCl is condensed, and therefore $\alpha = 1$. Within trial simulations, two metrics for the position of the peak were used: the position of the maximum of the peak and the the weighted average position between 3 and 5 Å. For $\epsilon_{MgRNA} = \epsilon_R$, both metrics suggest that $\sigma_{MgRNA} = 3.4$ Å yields a distribu-

tion most consistent with the outer-sphere peak observed in explicit-solvent simulations (Fig. 2).

To calibrate the Mg^{2+}-Mg^{2+} excluded volume, the Mg^{2+}-Mg^{2+} radial distribution function was used (Fig. S2). The radial distribution function rises sharply between 5 and 7 Å, and plateaus beyond this. $\sigma_{MgMg} = 5.6$ Å was found to most closely reproduce the midpoint of this rise.

Competition between Manning condensed Mg^{2+} and K^+ modulates the effective electrostatic potential

The Debye-Hückel potential assumes a linearized dependence of the Boltzmann distribution of ions on the electrostatic potential. Such an assumption is good far from the RNA, but breaks down near the RNA where the potential is large. Equation 6 uses Manning counterion condensation to account for the nonlinear effects in this region, so that the far-field potential is correct. The additional ions near the RNA deviating from linearity may be regarded as the Manning condensed counterions. Thus, the excess ions Γ may be split into a diffuse screening population and a condensed population close to the RNA.

Manning counterion condensation theory was originally derived for an infinite line of charge under limiting law conditions: as the salt concentration approaches zero while taking the thermodynamic limit. If the linear charge spacing (b) is shorter than the Bjerrum length (l_B – the length scale where the electrostatic and thermal energy scales cross), ions will condense out of solution onto the RNA. For an infinite line of charge, the number of ions per phosphate (θ) that condense is given by

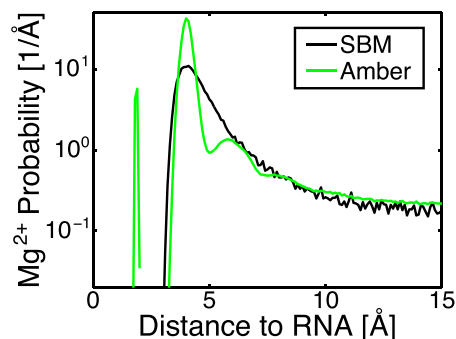$$\theta = \frac{1}{|Z|}\left(1 - \frac{1}{|Z|\xi}\right), \tag{9}$$

FIGURE 2 Comparison of the Mg^{2+} distribution about the SAM-I riboswitch in SBM and explicit-solvent Amber simulations. Distances to the closest RNA heavy atom were computed and binned. SBM captures well the general shape of the distribution, but misses the more subtle hydration features. The chelated ion at 2 Å could have been included in the SBM, but was omitted for simplicity. These curves were used to calibrate the excluded volume between Mg^{2+} and RNA atoms. The position of the maximum of the peak as well as the weighted average position between 3 and 5 Å both suggest that $\sigma_{MgRNA} = 3.4$ Å. To see this figure in color, go online.

where Z is the valency of the counterion, $\xi = l_B/b$, and

$$l_B = \frac{1}{4\pi\epsilon_0\epsilon k_B T}. \tag{10}$$

Grouping phosphate and condensed counterion charges together results in an effective rescaling of phosphate charges by $\alpha = 1 - Z\theta$.

If explicit ions are used, bare RNA charges should be used, because condensation is captured by the ions. However, if ions are only represented implicitly through an effective potential, effective RNA charges that are rescaled by α must be used to account for Manning condensation. Because Mg^{2+} in the model is explicit and KCl is implicit, the condensed K$^+$ per phosphate (θ_+) and condensed Mg^{2+} per phosphate (θ_{2+}) must be separated so that θ_+ can be included in the effective potential, V_{ES}. θ_{2+} and θ_+ can be separated by solving the system of equations

$$\ln\left(\frac{\theta_{2+}e}{C_{2+}V}\right) = 2\ln\left(\frac{\theta_+e}{C_+V}\right) \tag{11}$$

$$\ln\left(\frac{\theta_+e}{C_+V}\right) = (1 - \theta_+ - 2\theta_{2+})F, \tag{12}$$

describing competition between condensed Mg^{2+} and K$^+$ (78), where e is Euler's number. Equation 11 balances the entropic cost of localizing one Mg^{2+} ion with the cost of localizing two K$^+$ ions. V is the effective volume into which a condensed ion is localized, and together with the K$^+$ and Mg^{2+} concentrations, C_+ and C_{2+}, determines the entropic cost of localization. Equation 12 balances the entropic cost of localizing a condensed ion with the energy benefit. $k_B T F$ is the free energy per phosphate to assemble the phosphate charges from infinity to the native geometry, originally approximated as an infinite line, and thus depends on screening length l_D and RNA geometry. Computing F for an infinite line of charge (Eq. S11) and taking the appro-

priate limits in Eqs. 11 and 12 returns Eq. 9. The condensation is constant over a wide range of concentrations because both the entropic cost and F go like $\ln(1/C)$.

Manning counterion condensation may be applied to finite systems with the caveat that whereas the entropic cost of condensation goes like $\ln(1/C)$, F does not. Thus, as the concentration goes to zero, so does the condensation, and the condensation is not constant over a wide range of concentrations as it is for an infinite line of charge (Fig. 3 A). Equation 12 can be reexpressed as

$$\theta_{2+} = \frac{1}{2}(\theta_0 - \theta_+) - A\ln\left(\frac{\theta_+}{\theta_0}\right), \tag{13}$$

where θ_0 is the number of condensed K$^+$ per phosphate in the absence of Mg^{2+} and A is $1/2F$. θ_0 and A in principle depend on RNA geometry, l_D, and C_+ through their dependence on F. Note that in the region where K$^+$ and Mg^{2+} compete, $C_+ \gg C_{2+}$. Thus, for constant C_+, l_D is also approximately constant. Since our simulations remain in the native basin, RNA geometry is also constant, and θ_0 and A are constant as C_{2+} varies at a fixed KCl concentration.

Due to the difficulty of computing F, θ_0 and A are treated as fitting parameters, leaving only θ_+ and θ_{2+} free to vary with C_{2+}. NLPB calculations at fixed l_D corroborate the form of Eq. 13, but there is also a nonnegligible population of condensed Cl$^-$ (Fig. 3, B and C). This occurs because Debye-Hückel predicts a nonphysical negative concentration of Cl$^-$ near the RNA. To account for their effect on electrostatic interactions, these condensed Cl$^-$ must be subtracted from θ_+ in Eq. 6. Even if these condensed Cl$^-$ ions (θ_-) are subtracted from θ_+, the fit with Eq. 13 is still quite good. A can be estimated by fits to NLPB calculations (Fig. 3 C), but for this work, $A = 0$ is assumed for simplicity. Equation 13 then has the intuitive meaning that each additional condensed Mg^{2+} displaces two condensed
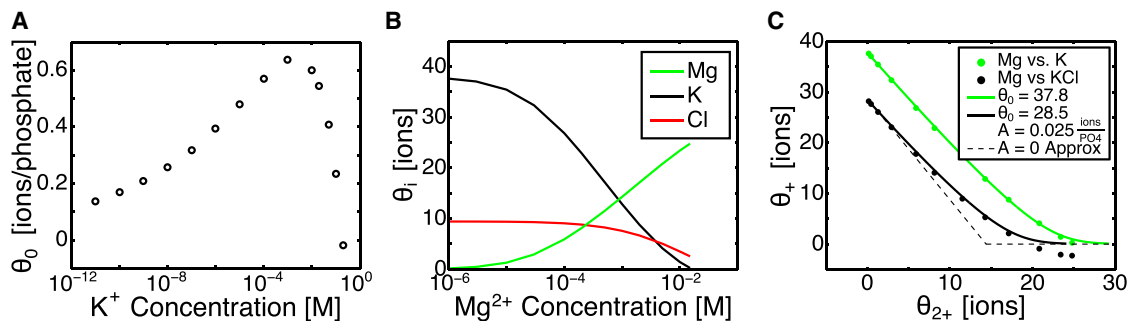

FIGURE 3   NLPB calculations of Manning condensation for the adenine riboswitch. (A) The Manning condensed ions obtained from NLPB in the absence of Mg^{2+} over a wide range of KCl concentrations. The Manning condensed fraction is not constant with concentration, as predicted by Manning theory for an infinite line of charge. (B) The Manning condensed ions partitioned into the three ionic species. The Debye length is held constant at the value for 50 mM KCl, whereas the Mg^{2+} level is increased. θ_{2+} increases with increasing Mg^{2+} concentration. (C) Competition between condensed Mg^{2+} and condensed K$^+$. Manning condensed ions from NLPB calculations are plotted along with fits to Eq. 13. Cl$^-$ is a nonnegligible portion of the condensed fraction. The fit to Eq. 13 is better if Cl$^-$ is ignored (green), but subtracting it from θ_+ (black) is more appropriate, so that the effect of condensed Cl$^-$ will be included in the effective electrostatic potential. A schematic of the $A = 0$ assumption (Eq. 14) is plotted as a dashed line. To see this figure in color, go online.

K$^+$. The effect of this assumption is most pronounced between medium and high C_{2+}, near $\theta_{2+} = \theta_0/2$.

To compute θ_+ in Eq. 6, an estimate of θ_{2+} is required. For nearly all the Mg^{2+} and K$^+$ concentrations considered, $C_+ \gg C_{2+}$. Thus, the screening is almost exclusively due to K$^+$ and Cl$^-$. Since the excess Mg^{2+} can be divided into a screening population, which is approximately zero, and a condensed population, any excess Mg^{2+} is condensed. This means Γ_{2+} is approximately equal to θ_{2+} (when both are expressed in units of ions per phosphate), and

$$\theta_+ = \begin{cases} \theta_0 - 2\Gamma_{2+} & \Gamma_{2+} < \frac{1}{2}\theta_0 \\ 0 & \Gamma_{2+} > \frac{1}{2}\theta_0. \end{cases} \qquad (14)$$

The approximate equality of Γ_{2+} and θ_{2+} is evidenced by the large population of Mg^{2+} in the outer-sphere regime and the near absence of diffuse Mg^{2+} observed in previous studies, even with a relatively high Mg^{2+} concentration (21).

To determine θ_+ for a particular Mg^{2+} concentration, an iterative, self-consistent approach is used. A value for θ_0 is chosen. After an initial guess for Γ_{2+} and subsequent calculation of θ_+ with Eq. 14, the simulation is run and Γ_{2+} is computed from the Mg^{2+} distribution and updated. The process is repeated until Γ_{2+} converges. The single remaining adjustable parameter, θ_0, was used to fit the experimental data for the adenine riboswitch and was estimated from NLPB methods for the SAM-I riboswitch.

SBMs capture excess Mg^{2+} and Mg^{2+}-RNA interaction free energy

With the Mg^{2+} excluded volume calibrated, and with a method for including Manning condensed KCl, we can compute preferential interaction coefficients and interaction free energies from simulation. The agreement with previous experimental data (39) and explicit-solvent data (21) is quite close (see Fig. 5), and suggests the model is well parameterized thermodynamically.

For the adenine riboswitch, Leipply and Draper performed fluorescence measurements down to very low Mg^{2+} concentrations (39), where Mg^{2+} competition with K$^+$ condensation is important. If condensed K$^+$ is neglected in our model, the fit to experimental data is good for high Mg^{2+} concentration where $\theta_+ = 0$, but poor for low Mg^{2+} concentration (Fig. 4). NLPB calculations estimate $\theta_0 = 28.4$ ions for the adenine riboswitch in 50 mM KCl. We find that $\theta_0 = 20$ ions (0.29 ions per phosphate) produces a much closer fit (Fig. 4). With this fitted K$^+$ condensation, it can be seen that the Mg^{2+}-RNA interaction free energy is within 8% at 1 mM Mg^{2+}, compared to the 25% typically observed with NLPB theory (75,76).

It is unclear whether the NLPB estimation and experimental fit of θ_0 disagree because the approximations or
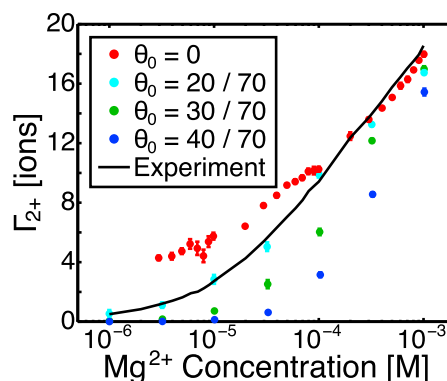

FIGURE 4 Comparison of preferential interaction coefficients of the adenine riboswitch at 50 mM KCl obtained for several choices of θ_0 to experimental data. Although NLPB estimates suggest that $\theta_0 = 28.4$ ions, $\theta_0 = 20$ ions provides a closer fit to the experimental data. Manning condensed K$^+$ cannot be neglected, as seen by the data for $\theta_0 = 0$. To see this figure in color, go online.

parameters of NLPB break down or because the fit of θ_0 is compensating for other neglected effects, such as hydration or nonuniform K$^+$ displacement. In either case, these discrepancies likely exist in the SAM-I system as well. Therefore, as an initial approximation, the NLPB estimate of θ_0 for the SAM-I riboswitch (25.7 ions) was scaled by the same ratio of 70% as observed for the adenine riboswitch to obtain $\theta_0 = 18$ ions (0.20 ions per phosphate).

An estimate of θ_0 was required for the SAM-I riboswitch because previous explicit solvent simulations could only be performed in a high Mg^{2+} concentration range (1–10 mM) where Mg^{2+} completely outcompetes K$^+$ condensation (i.e., $\theta_+ = 0$). Since $\theta_0 < \Gamma_{2+}$ for all three simulations, θ_0 cannot be constrained by a fit or adjusted to improve the fit. The agreement with previous explicit-solvent results for Γ_{2+} for these high Mg^{2+} concentrations is quite close. The KCl condensation and choice of θ_0 is of importance for low Mg^{2+} concentrations and for the computation of the free energy. Although no data exist for comparison, it would be useful to devise new experiments to test predictions and constrain θ_0. It should be noted that there is a chelated ion in SAM-I that was neglected in this study. This ion would likely raise Γ_{2+} near Mg^{2+} concentrations of 10^{-5} M, and would raise $\Delta G_{\text{Mg}^{2+}}$ by a few $k_B T$.

DISCUSSION

Model captures outer-sphere Mg^{2+} and can be extended for chelated Mg^{2+}

Although the outer-sphere population accounts for the majority of excess Mg^{2+} (21), Mg^{2+} chelation sites can have an effect on Γ_{2+} and $\Delta G_{\text{Mg}^{2+}}$. A chelated Mg^{2+} ion raises Γ_{2+} by nearly one ion at low Mg^{2+} concentrations, due to the typically high affinity of chelation sites. At higher Mg^{2+} concentrations, an absent chelated ion is largely

replaced by less tightly associated ions, and Γ_{2+} is independent of the presence of the chelated ion. A chelated ion affects $\Delta G_{Mg^{2+}}$ over all concentrations, because the integral over Γ_{2+} includes the lower concentrations, but the effect is generally small. For example, in one study, a chelation site became occupied near 2 μM and was shown to contribute several $k_B T$ to $\Delta G_{Mg^{2+}}$ (40). This contribution was only a small fraction of $\Delta G_{Mg^{2+}}$. Since most of $\Delta G_{Mg^{2+}}$ is due to outer-sphere Mg^{2+}, accurately representing outer-sphere Mg^{2+} is essential for a model of Mg^{2+}-RNA interactions. Although sometimes important, especially for $\Delta\Delta G_{Mg^{2+}}$, energetic contributions from chelated ions are a perturbation in comparison.

This model focuses on modeling outer sphere and diffuse Mg^{2+}. Previous work has demonstrated that for the SAM-I riboswitch, and likely for other RNAs of similar size, the outer-sphere population is dominant (21). That result is underscored here by the ability of this model to capture $\Delta G_{Mg^{2+}}$ and Γ_{2+} without chelated ions. For larger systems (62) or highly compact systems with buried phosphates (79), chelated ions are more important. Chelated ions have been included with harmonic restraints in the SBM without electrostatics (31). These techniques can be easily extended to this charged model by adding charge to the Mg^{2+} ion, and are quite adequate for native basin fluctuations. Further extensions to allow unbinding will be required for fluctuations outside the native basin or for computation of $\Delta G_{Mg^{2+}}$ in systems where chelated Mg^{2+} is important.

Mg²⁺-RNA interactions are sensitive to Manning condensed KCl

Manning theory, as formulated for an infinite line of charge, suggests that condensation is constant over a wide range of concentrations. Although this is correct for infinite lines of charge, the riboswitch systems considered in this work show substantial variation of the Manning condensed ions over the small range of physiologically relevant KCl concentrations (Fig. 3 A). As a result, θ_0 varies with KCl concentration and RNA geometry. The excess Mg^{2+}, and hence $\Delta G_{Mg^{2+}}$, are sensitive to θ_0 (Fig. 4). Thus, accurate methods for estimating θ_0 for the structures and concentrations of interest are critical for the accuracy of the hybrid SBM. Two methods were used to estimate θ_0: a fitting of the experimental HQS data and NLPB calculations. These methods disagree by eight ions, which is about 10% of the RNA charge. As mentioned in the third subsection under Results, the reasons for this disagreement are unclear but likely stem from either approximations or parameter choices in the NLPB calculation or from the θ_0 fit compensating for other effects neglected by the SBM.

It could be that NLPB does not capture θ_0 well because of the parameters used in the calculations, specifically the K^+ radius. Previous studies (75,76) have shown that standard

NLPB parameters underestimate Γ_{2+}, and from our experimental fit, the parameters also seem to overestimate θ_0. This suggests that RNA affinity for K^+ may be too high with these NLPB parameters. The K^+ affinity can be lowered by increasing the radius of K^+. Indeed, in NLPB theory, the ion radius is sometimes used as a fitting parameter (80). In the parameterization presented in this study, Mg^{2+} and K^+ have the same radius of 2.0 Å. For Mg^{2+}, this captures the hexahydrated size of Mg^{2+} well, but for K^+ this is larger than the bare radius, and smaller than the hydrated radius. Other standard NLPB parameters use a larger K^+ radius that corresponds to hydrated K^+, and argue against using a smaller radius because NLPB cannot capture several effects relevant to dehydrated ions (81). Simulations have shown that some K^+ dehydrates to associate with RNA (80), but this may be a force-field artifact, since NMR experiments suggest that K^+ does not dehydrate in the presence of RNA (82). As a result, it is unclear what K^+ radius is appropriate for NLPB calculations, but a larger radius may improve agreement with the fitted value for θ_0.

It is also possible that NLPB estimates of θ_0 differ from the experimental fit because the θ_0 fit compensates for other effects neglected by the hybrid SBM. θ_0 weakens Mg^{2+}-RNA interactions at low Mg^{2+} concentrations. Thus, if the hybrid SBM underpredicts Mg^{2+}-RNA affinity, especially at low Mg^{2+} concentrations, it will also underpredict θ_0 to compensate. Hydration is one possible neglected effect. In Fig. 2, the outer-sphere peak at 4 Å is higher for the explicit-solvent simulation (which includes hydration effects), than for the SBM. Although the area under the curves is nearly equal due to compensation by the width and height of the peak, the SBM slightly underpredicts Mg^{2+}-RNA affinity at high concentrations, as seen in Fig. 5, A and C). If this trend continues to low concentrations, the model will underpredict θ_0 to compensate. Another possible neglected effect is the nonuniform displacement of K^+. In the proposed SBM, condensed Mg^{2+} displaces K^+ uniformly by lowering θ_+, whereas in reality the K^+ is instead likely displaced from the immediate neighborhood of a Mg^{2+} ion, which could allow stronger interactions with the nearby phosphates.

The transferability of the model to other RNAs, other KCl concentrations, or other ionic species is of great interest. The form of the model is transferable, but results are sensitive to the specific value of the parameter θ_0. Transfer to other ionic species may be as simple as adjusting θ_0 for monovalent ions and σ_{MgRNA} and σ_{MgMg} for divalent ions (see Section S7 in the Supporting Material). A systematic way of predicting θ_0 is required to generalize the model to other KCl concentrations or other RNA systems where no experimental data exist for fitting. In this study, θ_0 could not be directly fit to experimental data for the SAM-I riboswitch. Since the experimental fit value for the adenine riboswitch was 70% of the NLPB estimate, the NLPB estimate of θ_0 was scaled by 70% in the SAM-I riboswitch as well.
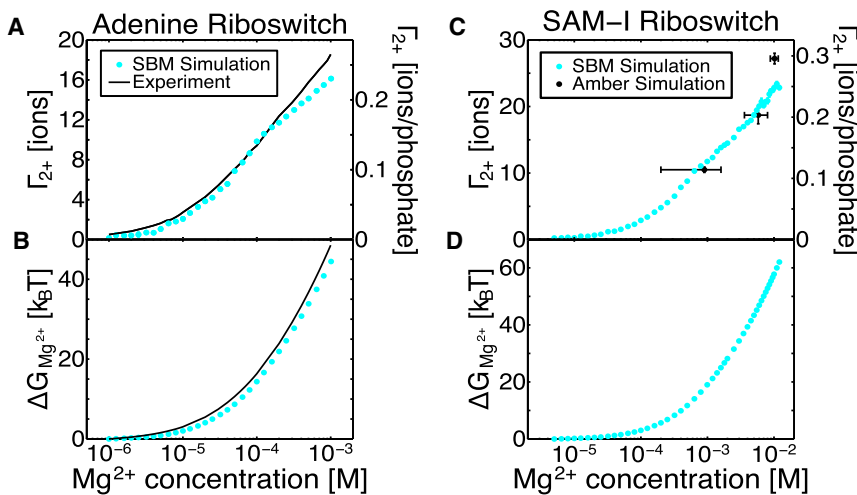
FIGURE 5 Excess Mg^{2+} (Γ_{2+}) and Mg^{2+}-RNA interaction free energy ($\Delta G_{Mg^{2+}}$) in the hybrid SBM with explicit Mg^{2+} agree with previous experimental and computational findings. Uncertainties from bootstrap analysis are plotted as error bars, but are too small to see in most cases. (A) Comparison between Γ_{2+} for the adenine riboswitch obtained in this study with SBM and a previous experimental fluorescence study (39). The 71 base RNA has a net charge of −70. KCl is present at 50 mM. Even at comparatively low concentrations, Mg^{2+} is able to effectively compete with K^+ and Cl^-. (B) The Mg^{2+} interaction free energy ($\Delta G_{Mg^{2+}}$) obtained from Eq. 1 by integrating Γ_{2+}. Agreement between the two curves suggests that SBMs with explicit Mg^{2+} are capable of capturing the energetic stabilization due to Mg^{2+}. (C) Comparison between Γ_{2+} for the SAM-I riboswitch obtained in this study with SBM and a previous Amber 99 molecular dynamics study (21). The 94 base RNA has a net charge of −92. KCl is present at 100 mM. Since θ_0 is 18 ions, all values of Γ_{2+} above 9 ions are unaffected by K^+ condensation. (D) Predicted $\Delta G_{Mg^{2+}}$ obtained by integrating Γ_{2+} of SAM-I. No data exist for comparison. To see this figure in color, go online.

Explicit solvent simulations could not confirm or refute the choice of θ_0 because the low Mg^{2+} concentrations involved are inaccessible. Thus, SBM simulations of several systems must be compared with HQS fluorescence measurements to learn how to predict θ_0. NLPB estimates may turn out to be the best method for estimating θ_0. NLPB estimates might be improved by adjusting the NLPB K^+ radius, or else the KCl concentration dependence NLPB estimate scaling factor, 70% here, could be probed. The tightly bound ion model (22) may give better results than NLPB. Alternatively, developing methods to compute the free energy, F, in Eq. 12 rather than fitting it may be fruitful. Models of θ_0 should be tested against fluorescent HQS titrations at several KCl concentrations. Such data already exist for an rRNA 58-mer (76), but new HQS titrations of other systems are of great interest.

Generalizing and applying the model

With the model of Mg^{2+}-RNA interactions presented here corroborated by previous experimental and computational studies, one can investigate the effects of Mg^{2+} upon the RNA energy landscape. Such models can explore the relative stability of various basins on the energy landscape as a function of ionic concentration, from the intermediates of riboswitch folding to functional transitions in the ribosome. In this study, we have computed $\Delta G_{Mg^{2+}}$ as a first step toward computing the differential Mg^{2+}-RNA interaction free energy between two ensembles, $\Delta\Delta G_{Mg^{2+}}$. $\Delta\Delta G_{Mg^{2+}}$ is the relevant biological quantity because it determines the Mg^{2+}-dependent free-energy difference between the two ensembles and thus the thermodynamic change in occupation probability as the ionic concentration changes. Several previous studies (75,76) have sought to compute $\Delta\Delta G_{Mg^{2+}}$

with NLPB, but the precision of these calculations is limited by large uncertainties in the partially unfolded ensemble, which was represented by a few static structural models. With the SBM approach, one can more fully sample the partially unfolded ensemble and probe how the ensemble changes with Mg^{2+} concentration, removing a large source of uncertainty in the NLPB approach.

As we move toward probing $\Delta\Delta G_{Mg^{2+}}$ between interconverting ensembles, care must be taken to ensure that the K^+ condensation, θ_+, does not radically change between ensembles. Since we only examine ensembles close to the crystal structure, this investigation is only able to check the θ_+ dependence on Mg^{2+} concentration. However, as expressed in Eq. 13, θ_+ can also depend on Mg^{2+} condensation for which concentration is a proxy, and on geometry and screening length, l_D, through the parameters A and θ_0. Fortunately, changes in θ_0 and θ_{2+} due to structural changes will have opposite effects on θ_+ and may largely cancel. If it turns out that K^+ condensation depends radically on structure, θ_+ can be made a time-dependent function of structural order parameters, likely through calculation of F in Eq. 12. Although this is undesirable from a modeling perspective, it is valid, since the relaxation time of the K^+ condensation is much faster than the Mg^{2+} dynamics.

The hybrid SBM will be a useful tool for addressing questions beyond $\Delta\Delta G_{Mg^{2+}}$. Cooperativity in Mg^{2+}-induced transitions can be quantified, and changes to transition states can be identified. Mg^{2+} is known to have a strong effect on RNA kinetics. This is due at least in part to higher barriers between states, but may also result from changes in diffusion due to coupling between Mg^{2+} and RNA dynamics. Extensive sampling of an SBM can partition the effect of Mg^{2+} on RNA kinetics into changing barrier height and diffusion. These effects will be quite interesting to examine in future investigations.

CONCLUSION

Structure-based models provide a baseline representation of the minimally frustrated landscape predicted by energy-landscape theory. Roughness, frustration, and nonspecific interactions such as electrostatics may be added to this baseline to determine their effects on RNA folding and function. To account for the ionic sensitivity and highly charged nature of RNA, we have extended an all-atom structure-based model to include electrostatic interactions with explicit Mg^{2+} and implicit KCl.

The excess Mg^{2+} is a powerful metric, which allows coupling of the SBM with fluorescence measurements and explicit-solvent simulations. The model was extensively parameterized and tested against previous explicit-solvent simulations and HQS fluorescence measurements of excess Mg^{2+}. Because of the close connection between excess Mg^{2+} and the Mg^{2+}-RNA interaction free energy, the agreement of the model with experiment suggests that the model is well parameterized to capture Mg^{2+}-RNA interaction free energies. The success of the hybrid SBM model, which is designed to capture the dynamics of the outer-sphere Mg^{2+} population, further corroborates the dominance of this population suggested by explicit-solvent simulations.

NLPB calculations suggest that for compact RNA structures, Manning condensed ions are not constant over a wide range of ionic concentrations as they are for lone RNA helices approximated by infinite lines of charge. Manning counterion condensation and competition between condensed populations is seen to be a critical correction to the Debye-Hückel approximation implemented here. A model of Mg^{2+}-RNA interactions must account for the effect of Manning condensed KCl.

The hybrid SBM opens up concentration regimes and timescales inaccessible to explicit-solvent simulation. With these models, one can explore the relative stability of basins of the energy landscape as a function of ion concentration. The effects of ions on kinetics through barrier height, transition states, and diffusion can also be investigated. SBMs are now poised to address complex questions about the interplay of Mg^{2+}, ligands, and RNA in folding and function.

SUPPORTING MATERIAL

Three figures, a detailed description of the model and methods, and references (83–86) are available at http://www.biophysj.org/biophysj/supplemental/S0006-3495(14)00145-3.

REFERENCES

1. Bryngelson, J. D., and P. G. Wolynes. 1987. Spin glasses and the statistical mechanics of protein folding. *Proc. Natl. Acad. Sci. USA.* 84:7524–7528.

2. Zwanzig, R., A. Szabo, and B. Bagchi. 1992. Levinthal's paradox. *Proc. Natl. Acad. Sci. USA.* 89:20–22.

3. Onuchic, J. N., Z. Luthey-Schulten, and P. G. Wolynes. 1997. Theory of protein folding: the energy landscape perspective. *Annu. Rev. Phys. Chem.* 48:545–600.

4. Ferreiro, D. U., J. A. Hegler, …, P. G. Wolynes. 2011. On the role of frustration in the energy landscapes of allosteric proteins. *Proc. Natl. Acad. Sci. USA.* 108:3499–3503.

5. Whitford, P. C., O. Miyashita, …, J. N. Onuchic. 2007. Conformational transitions of adenylate kinase: switching by cracking. *J. Mol. Biol.* 366:1661–1671.

6. Clementi, C., and S. S. Plotkin. 2004. The effects of nonnative interactions on protein folding rates: theory and simulation. *Protein Sci.* 13:1750–1766.

7. Oliveira, R. J., P. C. Whitford, …, V. B. P. Leite. 2010. The origin of nonmonotonic complex behavior and the effects of nonnative interactions on the diffusive properties of protein folding. *Biophys. J.* 99:600–608.

8. Weinkam, P., E. V. Pletneva, …, P. G. Wolynes. 2009. Electrostatic effects on funneled landscapes and structural diversity in denatured protein ensembles. *Proc. Natl. Acad. Sci. USA.* 106:1796–1801.

9. Azia, A., and Y. Levy. 2009. Nonnative electrostatic interactions can modulate protein folding: molecular dynamics with a grain of salt. *J. Mol. Biol.* 393:527–542.

10. Behrouzi, R., J. H. Roh, …, S. A. Woodson. 2012. Cooperative tertiary interaction network guides RNA folding. *Cell.* 149:348–357.

11. Rangan, P., B. Masquida, …, S. A. Woodson. 2004. Architecture and folding mechanism of the Azoarcus Group I Pre-tRNA. *J. Mol. Biol.* 339:41–51.

12. Marek, M. S., A. Johnson-Buck, and N. G. Walter. 2011. The shape-shifting quasispecies of RNA: one sequence, many functional folds. *Phys. Chem. Chem. Phys.* 13:11524–11537.

13. Thirumalai, D., and C. Hyeon. 2009. Chapter 2: Theory of RNA Folding: From Hairpins to Ribozymes. Springer, Berlin/Heidelberg.

14. Hyeon, C., J. Lee, …, D. Thirumalai. 2012. Hidden complexity in the isomerization dynamics of Holliday junctions. *Nat. Chem.* 4:907–914.

15. Draper, D. E. 2004. A guide to ions and RNA structure. *RNA.* 10:335–343.

16. Draper, D. E., D. Grilley, and A. M. Soto. 2005. Ions and RNA folding. *Annu. Rev. Biophys. Biomol. Struct.* 34:221–243.

17. Lambert, D., D. Leipply, …, D. E. Draper. 2009. The influence of monovalent cation size on the stability of RNA tertiary structures. *J. Mol. Biol.* 390:791–804.

18. Koculi, E., C. Hyeon, …, S. A. Woodson. 2007. Charge density of divalent metal cations determines RNA stability. *J. Am. Chem. Soc.* 129:2676–2682.

19. Heilman-Miller, S. L., D. Thirumalai, and S. A. Woodson. 2001. Role of counterion condensation in folding of the Tetrahymena ribozyme. I. Equilibrium stabilization by cations. *J. Mol. Biol.* 306:1157–1166.

20. Heilman-Miller, S. L., J. Pan, …, S. A. Woodson. 2001. Role of counterion condensation in folding of the Tetrahymena ribozyme. II. Counterion-dependence of folding kinetics. *J. Mol. Biol.* 309:57–68.

21. Hayes, R. L., J. K. Noel, …, K. Y. Sanbonmatsu. 2012. Magnesium fluctuations modulate RNA dynamics in the SAM-I riboswitch. *J. Am. Chem. Soc.* 134:12043–12053.

22. Chen, G., Z. J. Tan, and S.-J. Chen. 2010. Salt-dependent folding energy landscape of RNA three-way junction. *Biophys. J.* 98:111–120.

23. Hennelly, S. P., I. V. Novikova, and K. Y. Sanbonmatsu. 2013. The expression platform and the aptamer: cooperativity between Mg^{2+} and ligand in the SAM-I riboswitch. *Nucleic Acids Res.* 41:1922–1935.

24. Whitford, P. C., J. K. Noel, …, J. N. Onuchic. 2009. An all-atom structure-based potential for proteins: bridging minimal models with all-atom empirical forcefields. *Proteins.* 75:430–441.

25. Clementi, C., H. Nymeyer, and J. N. Onuchic. 2000. Topological and energetic factors: what determines the structural details of the transition state ensemble and "en-route" intermediates for protein folding? An investigation for small globular proteins. *J. Mol. Biol.* 298:937–953.

26. Hyeon, C., and J. N. Onuchic. 2007. Mechanical control of the directional stepping dynamics of the kinesin motor. *Proc. Natl. Acad. Sci. USA.* 104:17382–17387.

27. Sułkowska, J. I., J. K. Noel, and J. N. Onuchic. 2012. Energy landscape of knotted protein folding. *Proc. Natl. Acad. Sci. USA.* 109:17783–17788.

28. Hyeon, C., and D. Thirumalai. 2005. Mechanical unfolding of RNA hairpins. *Proc. Natl. Acad. Sci. USA.* 102:6789–6794.

29. Cho, S. S., D. L. Pincus, and D. Thirumalai. 2009. Assembly mechanisms of RNA pseudoknots are determined by the stabilities of constituent secondary structures. *Proc. Natl. Acad. Sci. USA.* 106:17349–17354.

30. Whitford, P. C., A. Schug, …, K. Y. Sanbonmatsu. 2009. Nonlocal helix formation is key to understanding S-adenosylmethionine-1 riboswitch function. *Biophys. J.* 96:L7–L9.

31. Whitford, P. C., P. Geggier, …, K. Y. Sanbonmatsu. 2010. Accommodation of aminoacyl-tRNA into the ribosome involves reversible excursions along multiple pathways. *RNA.* 16:1196–1204.

32. Ratje, A. H., J. Loerke, …, C. M. T. Spahn. 2010. Head swivel on the ribosome facilitates translocation by means of intra-subunit tRNA hybrid sites. *Nature.* 468:713–716.

33. Whitford, P. C., A. Ahmed, …, K. Y. Sanbonmatsu. 2011. Excited states of ribosome translocation revealed through integrative molecular modeling. *Proc. Natl. Acad. Sci. USA.* 108:18943–18948.

34. Hamelberg, D., T. Shen, and J. A. McCammon. 2006. Insight into the role of hydration on protein dynamics. *J. Chem. Phys.* 125:094905.

35. Zwanzig, R. 1988. Diffusion in a rough potential. *Proc. Natl. Acad. Sci. USA.* 85:2029–2030.

36. Kouza, M., M. S. Li, …, D. Thirumalai. 2006. Effect of finite size on cooperativity and rates of protein folding. *J. Phys. Chem. A.* 110:671–676.

37. Grilley, D., A. M. Soto, and D. E. Draper. 2006. Mg^{2+}-RNA interaction free energies and their relationship to the folding of RNA tertiary structures. *Proc. Natl. Acad. Sci. USA.* 103:14003–14008.

38. Leipply, D., and D. E. Draper. 2010. Dependence of RNA tertiary structural stability on Mg^{2+} concentration: interpretation of the Hill equation and coefficient. *Biochemistry.* 49:1843–1853.

39. Leipply, D., and D. E. Draper. 2011. Effects of Mg^{2+} on the free energy landscape for folding a purine riboswitch RNA. *Biochemistry.* 50:2790–2799.

40. Leipply, D., and D. E. Draper. 2011. Evidence for a thermodynamically distinct Mg^{2+} ion associated with formation of an RNA tertiary structure. *J. Am. Chem. Soc.* 133:13397–13405.

41. Chen, B., X. Zuo, …, T. K. Dayie. 2012. Multiple conformations of SAM-II riboswitch detected with SAXS and NMR spectroscopy. *Nucleic Acids Res.* 40:3117–3130.

42. Haller, A., U. Rieder, …, R. Micura. 2011. Conformational capture of the SAM-II riboswitch. *Nat. Chem. Biol.* 7:393–400.

43. Bastet, L., A. Dubé, …, D. A. Lafontaine. 2011. New insights into riboswitch regulation mechanisms. *Mol. Microbiol.* 80:1148–1154.

44. Priyakumar, U. D., and A. D. MacKerell, Jr. 2010. Role of the adenine ligand on the stabilization of the secondary and tertiary interactions in the adenine riboswitch. *J. Mol. Biol.* 396:1422–1438.

45. Banás, P., N. G. Walter, …, M. Otyepka. 2010. Protonation states of the key active site residues and structural dynamics of the glmS riboswitch as revealed by molecular dynamics. *J. Phys. Chem. B.* 114:8701–8712.

46. Doshi, U., J. M. Kelley, and D. Hamelberg. 2012. Atomic-level insights into metabolite recognition and specificity of the SAM-II riboswitch. *RNA.* 18:300–307.

47. Huang, W., J. Kim, …, F. Aboul-ela. 2013. The impact of a ligand binding on strand migration in the SAM-I riboswitch. *PLOS Comput. Biol.* 9:e1003069.

48. Lin, J.-C., and D. Thirumalai. 2008. Relative stability of helices determines the folding landscape of adenine riboswitch aptamers. *J. Am. Chem. Soc.* 130:14080–14081.

49. Serganov, A., Y.-R. Yuan, …, D. J. Patel. 2004. Structural basis for discriminative regulation of gene expression by adenine- and guanine-sensing mRNAs. *Chem. Biol.* 11:1729–1741.

50. Lemay, J.-F., J. C. Penedo, …, D. A. Lafontaine. 2006. Folding of the adenine riboswitch. *Chem. Biol.* 13:857–868.

51. Noeske, J., H. Schwalbe, and J. Wöhnert. 2007. Metal-ion binding and metal-ion induced folding of the adenine-sensing riboswitch aptamer domain. *Nucleic Acids Res.* 35:5262–5273.

52. Montange, R. K., and R. T. Batey. 2006. Structure of the S-adenosylmethionine riboswitch regulatory mRNA element. *Nature.* 441:1172–1175.

53. Stoddard, C. D., R. K. Montange, …, R. T. Batey. 2010. Free state conformational sampling of the SAM-I riboswitch aptamer domain. *Structure.* 18:787–797.

54. Huang, W., J. Kim, …, F. Aboul-ela. 2009. A mechanism for S-adenosyl methionine assisted formation of a riboswitch conformation: a small molecule with a strong arm. *Nucleic Acids Res.* 37:6528–6539.

55. Noel, J. K., P. C. Whitford, …, J. N. Onuchic. 2010. SMOG@ctbp: simplified deployment of structure-based models in GROMACS. *Nucleic Acids Res.* 38 (Web Server issue):W657–W661.

56. Denesyuk, N. A., and D. Thirumalai. 2013. Coarse-grained model for predicting RNA folding thermodynamics. *J. Phys. Chem. B.* 117:4901–4911.

57. Manning, G. S. 1978. The molecular theory of polyelectrolyte solutions with applications to the electrostatic properties of polynucleotides. *Q. Rev. Biophys.* 11:179–246.

58. Manning, G. S. 2002. Electrostatic free energy of the DNA double helix in counterion condensation theory. *Biophys. Chem.* 101-102:461–473.

59. Chu, V. B., Y. Bai, …, S. Doniach. 2007. Evaluation of ion binding to DNA duplexes using a size-modified Poisson-Boltzmann theory. *Biophys. J.* 93:3202–3209.

60. Moreira, A. G., and R. R. Netz. 2000. Strong-coupling theory for counter-ion distributions. *Europhys. Lett.* 52:705–711.

61. Noel, J. K., P. C. Whitford, and J. N. Onuchic. 2012. The shadow map: a general contact definition for capturing the dynamics of biomolecular folding and function. *J. Phys. Chem. B.* 116:8692–8702.

62. Klein, D. J., P. B. Moore, and T. A. Steitz. 2004. The contribution of metal ions to the structural stability of the large ribosomal subunit. *RNA.* 10:1366–1379.

63. Wang, J., P. Cieplak, and P. A. Kollman. 2000. How well does a restrained electrostatic potential (RESP) model perform in calculating conformational energies of organic and biological molecules? *J. Comput. Chem.* 21:1049–1074.

64. Hess, B., C. Kutzner, …, E. Lindahl. 2008. GROMACS 4: algorithms for highly efficient load-balanced, and scalable molecular simulation. *J. Chem. Theory Comput.* 4:435–447.

65. Honig, B., and A. Nicholls. 1995. Classical electrostatics in biology and chemistry. *Science.* 268:1144–1149.

66. Chen, S. W., and B. Honig. 1997. Monovalent and divalent salt effects on electrostatic free energies defined by the nonlinear Poisson-Boltzmann equation: application to DNA binding reactions. *J. Phys. Chem. B.* 101:9113–9118.

67. Manning, G. S., and U. Mohanty. 1997. Counterion condensation on ionic oligomers. *Physica A.* 247:196–204.

68. Baker, N. A., D. Sept, …, J. A. McCammon. 2001. Electrostatics of nanosystems: application to microtubules and the ribosome. *Proc. Natl. Acad. Sci. USA.* 98:10037–10041.

69. Baker, N. A. 2005. Improving implicit solvent simulations: a Poisson-centric view. *Curr. Opin. Struct. Biol.* 15:137–143.

70. Baker, N. A. 2004. Poisson-Boltzmann methods for biomolecular electrostatics. *Methods Enzymol.* 383:94–118.

71. He, Z., and S.-J. Chen. 2012. Predicting ion-nucleic acid interactions by energy landscape-guided sampling. *J. Chem. Theory Comput.* 8:2095–2101.

72. Boschitsch, A. H., and P. V. Danilov. 2012. Formulation of a new and simple nonuniform size-modified Poisson-Boltzmann description. *J. Comput. Chem.* 33:1152–1164.

73. Borukhov, I., and D. Andelman. 1997. Steric effects in electrolytes: a modified Poisson-Boltzmann equation. *Phys. Rev. Lett.* 79:435–438.

74. Misra, V. K., and D. E. Draper. 2001. A thermodynamic framework for Mg^{2+} binding to RNA. *Proc. Natl. Acad. Sci. USA.* 98:12456–12461.

75. Soto, A. M., V. Misra, and D. E. Draper. 2007. Tertiary structure of an RNA pseudoknot is stabilized by "diffuse" Mg^{2+} ions. *Biochemistry.* 46:2973–2983.

76. Grilley, D., V. Misra, …, D. E. Draper. 2007. Importance of partially unfolded conformations for Mg^{2+}-induced folding of RNA tertiary structure: structural models and free energies of Mg^{2+} interactions. *Biochemistry.* 46:10266–10278.

77. Savelyev, A., and G. A. Papoian. 2008. Polyionic charge density plays a key role in differential recognition of mobile ions by biopolymers. *J. Phys. Chem. B.* 112:9135–9145.

78. Wilson, R. W., D. C. Rau, and V. A. Bloomfield. 1980. Comparison of polyelectrolyte theories of the binding of cations to DNA. *Biophys. J.* 30:317–325.

79. Draper, D. E. 2013. Folding of RNA tertiary structure: Linkages between backbone phosphates, ions, and water. *Biopolymers.* 99:1105–1113.

80. Kirmizialtin, S., A. R. Silalahi, …, M. O. Fenley. 2012. The ionic atmosphere around A-RNA: Poisson-Boltzmann and molecular dynamics simulations. *Biophys. J.* 102:829–838.

81. Chen, A. A., M. Marucho, …, R. V. Pappu. 2009. Simulations of RNA interactions with monovalent ions. *Methods Enzymol.* 469: 411–432.

82. Braunlin, W. H. 1995. NMR studies of cation-binding environments on nucleic acids. *Adv. Phys. Chem.* 5:89–139.

83. Tsai, J., R. Taylor, …, M. Gerstein. 1999. The packing density in proteins: standard radii and volumes. *J. Mol. Biol.* 290:253–266.

84. Perel, V., and B. Shklovskii. 1999. Screening of a macroion by multi-valent ions: a new boundary condition for the Poisson-Boltzmann equation and charge inversion. *Physica A.* 274:446–453.

85. Eisenhaber, F., P. Lijnzaad, …, M. Scharf. 1995. The double cubic lattice method: efficient approaches to numerical integration of surface area and volume and to dot surface contouring of molecular assemblies. *J. Comput. Chem.* 16:273–284.

86. Auffinger, P., N. Grover, and E. Westhof. 2011. Metal ion binding to RNA. *Met. Ions Life Sci.* 9:1–35.